

and stringent constraints claimed by Ref. [21] and commented by Refs. [22, 23]. All of these show that it is still very much an open debate and no concrete conclusions can be drawn yet, without tackling this problem from every possible angle (also see Ref. [24] for the most recent stringent limits).

One way to further investigate this open problem is to use upcoming X-ray telescopes such as eROSITA [25], XRISM [26], and Athena [27]. In this paper, we study sensitivities of these telescopes to the sterile neutrino decay. XRISM and Athena have superb energy resolution that is ideal for line searches, while eROSITA enables the all-sky survey. They will provide a deeper look needed to potentially end this debate.

B. Heavy dark matter

The dark matter can be much heavier than GeV–TeV — typical mass scales of the WIMP dark matter. This makes an interesting possibility to be tested in light of current and upcoming data of TeV gamma-ray (HAWC [28], CTA [29], and LHAASO [30]) and TeV–PeV neutrino telescopes (IceCube [7], IceCube-Gen2 [31], KM3NeT [31, 32]).

For dark matter in a mass range of 1 TeV–10 PeV, the most stringent constraints on the decay lifetime of these particles was obtained by the Fermi Large Area Telescope, which are in the range of 10^{28} – 10^{29} s (see Ref. [6] and references therein).

These limits can be further improved with current and next generation TeV gamma-ray telescopes. HAWC features a wide field of view, and detects both gamma-rays and cosmic rays in an energy range between ~ 500 GeV and a few hundred TeV [33]. It consists of 300 water Cherenkov tanks that detect particles from air showers. CTA is a next-generation gamma-ray and cosmic ray observatory. Its field of view is up to 10° . It consists of two parts, indicated as CTA North and CTA South, which are complementary to each other for the sky coverage. It will cover a broad energy range from about 20 GeV to 300 TeV [29]. The Large High Altitude Air Shower Observatory (LHAASO) [30] is a near-future wide field of view gamma-ray observatory that is nearly completed [34, 35], which will be sensible to gamma rays in the range between 300 GeV and 1 PeV. Compared with other gamma-ray observatories, LHAASO will also have improved sensitivities above 50 TeV. In this work, we focus on the prospects with HAWC and CTA.

C. Dwarf spheroidal galaxies

dSphs provide a good environment to test the particle nature of dark matter. Due to its proximity and relatively dense environments, they can be one of the best places to indirectly look for dark matter non-gravitational interactions, such as decay into X-ray or

gamma-ray photons. In addition, because of the paucity of stars, gas, and any other baryonic components, if any signals were detected, they would hardly be coming from astrophysical components, hence making them an ideal target for dark matter searches.

In this paper, we make predictions for constraints on dark matter decay using current and future generation of telescopes of both X-rays and gamma rays, focusing on sterile neutrinos and heavy dark matter, respectively. We will study implications by using both the currently known dSphs and those that would be discovered by future surveys such as Vera C. Rubin Observatory Legacy Survey of Space and Time (LSST) (www.lsst.org). The LSST will cover the entire southern sky and find dozens of new dSphs [36, 37].

The rate of dark matter decay depends on the density profiles of dSphs. By applying theories of structure formation to the evolution of subhalos and satellites, Ref. [38] revised the estimate of density profiles of known dwarf galaxies. The effect was found substantial in terms of rates of WIMP annihilation, by lowering the previous estimates on upper limits to the annihilation cross section by a factor of 2–7. The same consideration will also reduce the decay rates. By using the same subhalo and satellite models, we are able to predict dSphs that would be discovered with the LSST, and also their density profiles [37]. Assessing these quantitatively and also giving the most precise estimates for the current and future indirect dark matter search strategies of various wavebands with all the dSphs are the goals of this work.

The rest of the paper is organized as follows. In Sec. II, we briefly introduce essential formulae in order to calculate the X-ray and gamma-ray flux from dark matter decay in dSphs. Section III discusses distributions of decay rates in known dSphs (Sec. III A) and LSST dSphs (Sec. III B), investigating dependence on various parameters related to dSph formation in dark matter subhalos. Our main results about the sensitivities of X-ray and gamma-ray telescopes are discussed in Secs. IV and V for sterile neutrinos and heavy dark matter, respectively. We then conclude the paper in Sec. VI.

II. DARK MATTER DECAYS IN DWARF GALAXIES

The differential flux of photons from dark matter decay from a sky region with a solid angle $\Delta\Omega$ is given by

$$\frac{dF}{dE} = \frac{\Gamma_\chi}{4\pi m_\chi} \frac{dN_{\text{decay}}}{dE} D, \quad (1)$$

where m_χ and Γ_χ are the mass and decay width of dark matter particle χ , respectively, and dN_{decay}/dE is the energy spectrum of the particle of interest per decay. The decay lifetime τ_χ is related to Γ_χ via $\tau_\chi = \Gamma_\chi^{-1}$. The flux is proportional to the so-called astrophysical D factor:

$$D_{\text{dSph}} = \int_{\Delta\Omega} d\Omega \int d\ell \rho_\chi(r(\ell, \psi)), \quad (2)$$

where $d\Omega = 2\pi \sin\psi d\psi$ and ψ is an angle coordinate subtending from the center of the dSph. We assume that the dark matter density is approximated by a spherically-symmetric Navarro-Frenk-White (NFW) profile [39]:

$$\rho_\chi(r) = \frac{\rho_s}{(r/r_s)(r/r_s + 1)^2}, \quad (3)$$

up to a tidal truncation radius r_t , beyond which $\rho_\chi = 0$. Therefore, density profiles for each dwarf galaxy are characterized by three parameters: r_s , ρ_s , and r_t . For each set of (r_s, ρ_s, r_t) and the integration angle α_{int} , we compute the D factor using a fitting formula found by Ref. [40] as follows:

$$D_{\text{dSph}} = \frac{4\pi\rho_s r_s^3}{d^2} \left[\ln \left(\frac{\min[\alpha_{\text{int}}d, r_t]}{2r_s} \right) + X \left(\frac{\min[\alpha_{\text{int}}d, r_t]}{r_s} \right) \right], \quad (4)$$

where d is a distance to the dSph, and

$$X(s) = \begin{cases} \text{arcsech } s/\sqrt{1-s^2}, & 0 \leq s \leq 1, \\ \text{arcsec } s/\sqrt{s^2-1}, & s \geq 1. \end{cases} \quad (5)$$

We also note that the D factor in Eq. (1) has another contribution from the smooth Galactic halo component. It can be computed by the same formulae, Eqs. (2) and (3), but with specific input parameters like $r_s = 20$ kpc, r_t set to be the virial radius $R_\odot = 200$ kpc, and ρ_s chosen to yield the local dark matter density of 0.4 GeV cm^{-3} at Galactocentric radius of the solar system, $r = R_\odot = 8.5$ kpc [41]. In order to obtain the D factor from the Milky-Way halo component, D_{MW} , we first calculate the line-of-sight integral of ρ_χ at a specific position in the sky of central coordinate of the dSph and then multiply it by the solid angle $\Delta\Omega$. For this, we evaluate the Galactocentric radius r as a function of the line-of-sight coordinate ℓ and the dSph's sky location ψ as

$$r = \sqrt{R_\odot^2 + \ell^2 - 2R_\odot\ell \cos\psi}. \quad (6)$$

The total D factor for the dwarf is then obtained as $D = D_{\text{dSph}} + D_{\text{MW}}$.

III. DISTRIBUTION OF DWARF D FACTOR

A. Dark matter decay in known dwarfs

The density profile of the dwarf galaxies are obtained through stellar kinematics observations (e.g., [42]). However, especially for ultrafaint dwarf galaxies, where there are not enough data, prior distributions of density profile parameters such as r_s and ρ_s have to be adopted in order to obtain their meaningful constraints in the Bayesian parameter inference. Often in the literature,

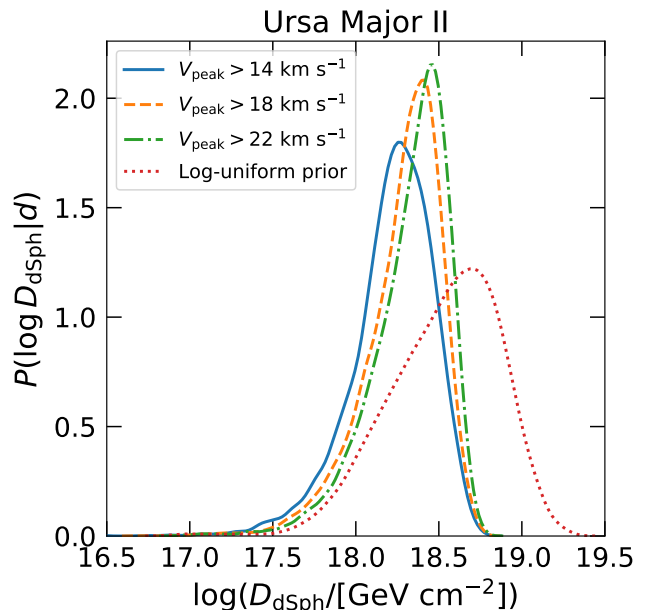


FIG. 1. Posterior probability distributions of $D_{\text{dSph}}(0.5^\circ)$ for Ursa Major II, obtained with satellite priors with $V_{\text{peak}} > 14 \text{ km s}^{-1}$ (solid), $V_{\text{peak}} > 18 \text{ km s}^{-1}$ (dashed), $V_{\text{peak}} > 22 \text{ km s}^{-1}$ (dot-dashed), and log-uniform priors (dotted).

non-informative priors — i.e., uniform distributions for both $\ln r_s$ and $\ln \rho_s$ — were used (e.g., [43]).

Instead, in this paper, we follow the procedure in Ref. [37] to estimate the density profile of observed dwarf galaxies, and also the expected distribution of dwarf D factors. The procedure employs subhalo models that account for their accretion onto the Milky-Way host halo at given redshift and mass, followed by tidal stripping after accretion. The model employed here was developed semi-analytically in Ref. [44], which was calibrated to the results of the N-body numerical simulations [45, 46]. We adopt the analysis results of Ref. [38] to obtain the posterior distribution of (r_s, ρ_s, r_t) for each known dwarf galaxy. Then the distribution of D factors for each dwarf is computed by using Eq. (4). However, there still remains a source of uncertainty within this prior modelling approach, which is connected to the condition that a satellite galaxy forms in a subhalo. We parameterize this with the peak value of the maximum circular velocity in the subhalo at the satellite formation, V_{peak} . We adopt $V_{\text{peak}} > 14 \text{ km s}^{-1}$ as the canonical condition, but investigate a range of different values and their impact on the results. For classical dSphs such as Draco, we instead adopt $V_{\text{peak}} > 25 \text{ km s}^{-1}$ prior [38]. Lastly, we compute the Milky-Way halo contribution, D_{MW} , based on the sky locations of each of the known dwarfs.

The resulting D -factor distributions for the different prior assumptions studied here are presented in Fig. 1 for the ultrafaint dSph, Ursa Major II. We find that physically motivated priors yield narrower posterior distributions with smaller median than the uninformative

prior, as found in Ref. [38]. Median and 68% credible regions for $\log(D_{\text{dSphs}}/[\text{GeV cm}^{-2}])$ integrated out to 0.5° with these posteriors are $18.25_{-0.26}^{+0.20}$ ($V_{\text{peak}} > 14 \text{ km s}^{-1}$), $18.32_{-0.25}^{+0.17}$ ($V_{\text{peak}} > 18 \text{ km s}^{-1}$), $18.38_{-0.28}^{+0.16}$ ($V_{\text{peak}} > 22 \text{ km s}^{-1}$), and $18.58_{-0.38}^{+0.30}$ (log-uniform prior). We also note that, for the Ursa Major II, the Milky-Way halo contribution gives $\sim 60\%$ of the total D factor. If D_{dSph} is obtained by integrating up to 0.05° instead, the corresponding median and 68% credible regions for $\alpha_{\text{int}} = 0.05^\circ$ are $16.75_{-0.17}^{+0.15}$ ($V_{\text{peak}} > 14 \text{ km s}^{-1}$), $16.80_{-0.15}^{+0.13}$ ($V_{\text{peak}} > 18 \text{ km s}^{-1}$), $16.83_{-0.14}^{+0.13}$ ($V_{\text{peak}} > 22 \text{ km s}^{-1}$), and $17.00_{-0.19}^{+0.17}$ (log-uniform prior). In this case, given that the NFW profile features central cusp, the contribution from the dSph is more important, with the fractional contribution from the Milky-Way halo decreases to about $\sim 30\%$.

The medians and the 68% and 95% credible intervals of these same priors for all the known ultrafaint dwarf galaxies are displayed in Fig. 2. There we observe overall similar features as for Fig. 1, with sharper predictions from informative priors and a moderate trend of smaller D -factor estimates compared with uninformative prior.

The medians and both 68% and 95% credible intervals for all the ultrafaint dSphs studied in this work is summarized in Fig. 2. One can see a general trend that the satellite priors yield systematically smaller D_{dSph} , whereas the effect is not as prominent as in the case of the annihilation studied in Ref. [38]. The results of D_{dSph} distributions of all the dSphs are also discussed in Appendix A in greater details.

B. Dark matter decay in LSST dwarfs

LSST will discover many more ultrafaint dwarf galaxies from the entire southern sky. Many of the known dSphs are found in the northern sky, and the LSST will therefore be able to complement this by searching for many more faint dSphs in the southern sky that is largely unexplored yet. Bright and nearby dwarfs in the southern sky may help further constrain models for indirect dark matter signals [37]. In order to obtain a D -factor distribution of these potential dSphs and then to estimate detectability of signals from decaying dark matter, it is necessary to obtain both a spatial distribution and a distribution of expected subhalo properties. While Ref. [37] explored the dark matter annihilation (and the so-called J factor), the procedure for modeling the subhalos and their satellite galaxies is similar to the one described in the previous subsection. As for the spatial distribution, we adopt the results of the hydrodynamical simulations of Ref. [47], combined with the correction for baryonic disruption and completeness effects from Ref. [48].

However, several assumptions have to be made in order to connect the subhalos and their satellite galaxies with given luminosity. We implement a cutoff on the V -band surface brightness that corresponds to the LSST

sensitivity, and also V_{peak} corresponding to the formation threshold for dSphs. As in the previous subsection, the canonical value for V_{peak} threshold is taken to be 14 km s^{-1} , below which dSphs are assumed not to form.

In Figs. 3 and 4, we show cumulative distribution of D_{dSph} from the *all sky*, $N(> D_{\text{dSph}})$ by varying thresholds for the V -band surface brightness (μ_V) and V_{peak} , respectively. The surface brightness condition of $\mu_V < 32 \text{ mag arcsec}^{-2}$ corresponds to the expectation for the LSST Year 1 data. We show Poisson uncertainties of these distributions (both 1σ and 2σ levels) as grey bands, with uncertainties calculated as $\sigma_N = \sqrt{N(> D)}$. We also included a cumulative distribution of all known dSph D factors (median values obtained in the previous subsection for $V_{\text{peak}} > 14 \text{ km s}^{-1}$), overlaid in these two figures. We note that the cumulative distribution of the known dSphs follows closely our predictions for the LSST dSphs, in good agreement within the Poisson errors at large- D regime.

For $\mu_V < 34 \text{ mag arcsec}^{-2}$ and $V_{\text{peak}} > 14 \text{ km s}^{-1}$, the mean number of dSphs in the all sky is ~ 100 . We first generate the number of subhalos that satisfy this condition through Monte Carlo simulation following the Poisson distribution with this mean. Then, following the D_{dSph} distribution, we assign D_{dSph} values to each of these mock dSphs. We also generate the sky location for each of these dSphs based on the column density of subhalos along each direction. If they are in the survey footprint of the LSST (i.e., declination smaller than 5 degrees), the dSph will be discovered with the LSST.

In addition to this, based on the sky location of each LSST dSph, we compute the Milky Way component of the D factor, D_{MW} . The relative contribution of this component to the total D factor depends strongly on the integration angle α_{int} . In Fig. 5, we show composition of the D factors for two values of the integration angle. For $\alpha_{\text{int}} = 0.5^\circ$ a large fraction of the dSph D factors are nearly indistinguishable from the Milky-Way component, while for $\alpha_{\text{int}} = 0.05^\circ$, we see that most dSph D factors are strongly separated from the Milky-Way component.

IV. STERILE NEUTRINO DARK MATTER

Sterile neutrinos communicate with the standard model only via mixing with active left-handed neutrino species. The conversion probability of a sterile neutrino into an active neutrino is proportional to $\sin^2 2\theta$, where θ is the mixing angle. The relation between the sterile neutrino decay width $\Gamma_{\nu_s} (= \tau_{\nu_s}^{-1})$ and mixing angle is (e.g., [3])

$$\Gamma_{\nu_s}(m_{\nu_s}, \theta) = 1.38 \times 10^{-29} \text{ s}^{-1} \left(\frac{\sin^2 2\theta}{10^{-7}} \right) \left(\frac{m_{\nu_s}}{1 \text{ keV}} \right)^5. \quad (7)$$

The X-ray flux is given by Eq. (1), and as the X-ray photons are produced through the decay process $\nu_s \rightarrow \nu_e + \gamma$, the energy spectrum per decay dN_{decay}/dE is a

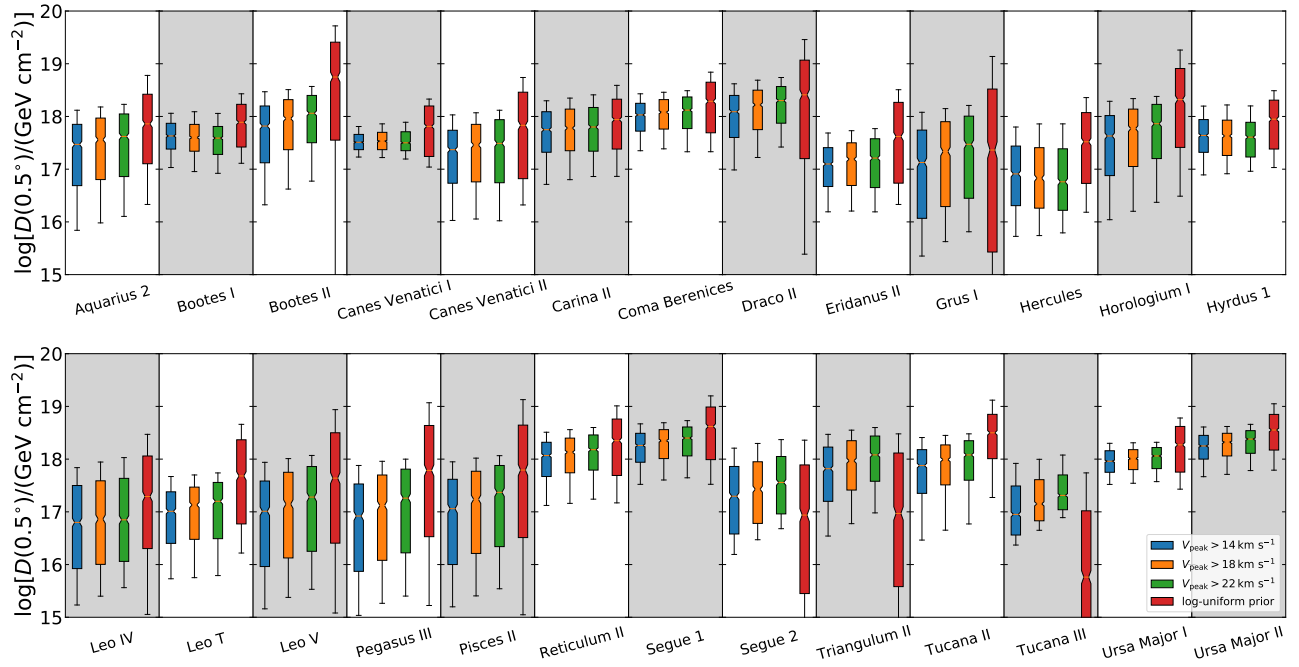


FIG. 2. Box-whisker diagram displaying the median and 68% (boxes) and 95% (whiskers) credible intervals of the D -factor posterior distribution for ultrafaint dSphs, with the integration angle up to 0.5° . The intervals corresponding to the four satellite priors considered in this research are presented as $V_{\text{peak}} > 14 \text{ km s}^{-1}$ (blue), $V_{\text{peak}} > 18 \text{ km s}^{-1}$ (orange), $V_{\text{peak}} > 22 \text{ km s}^{-1}$ (green), and log-uniform (red).

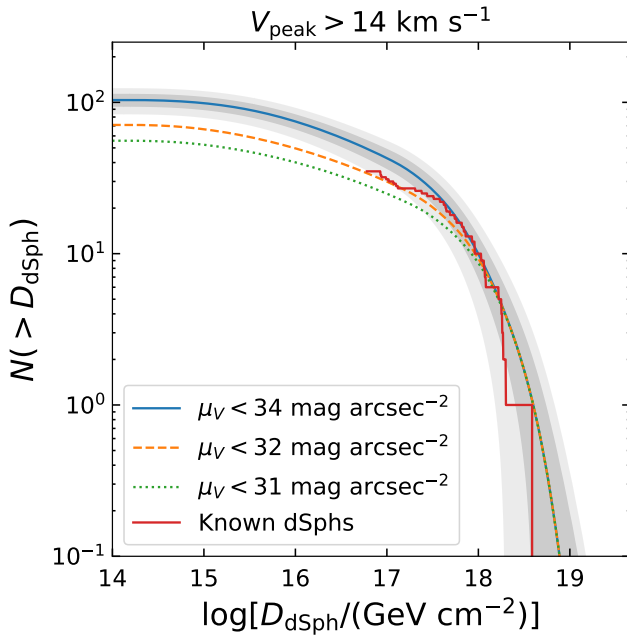


FIG. 3. Cumulative number of all-sky satellite dSphs with $V_{\text{peak}} > 14 \text{ km s}^{-1}$ for a few values of μ_V threshold. The grey shaded region represents the Poisson errors at 1σ and 2σ levels. The distribution of median D_{dSph} values of the known dSphs is also shown for comparison.

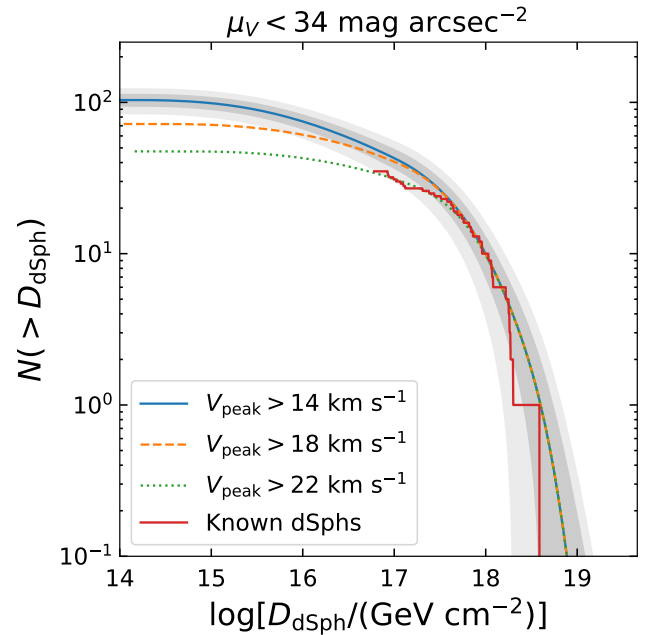


FIG. 4. The same as Fig. 3 but for $\mu_V < 34 \text{ mag arcsec}^{-2}$ and various values of V_{peak} threshold.

delta function:

$$\frac{dN_{\text{decay}}}{dE} = \delta\left(E - \frac{m_{\nu_s}}{2}\right). \quad (8)$$

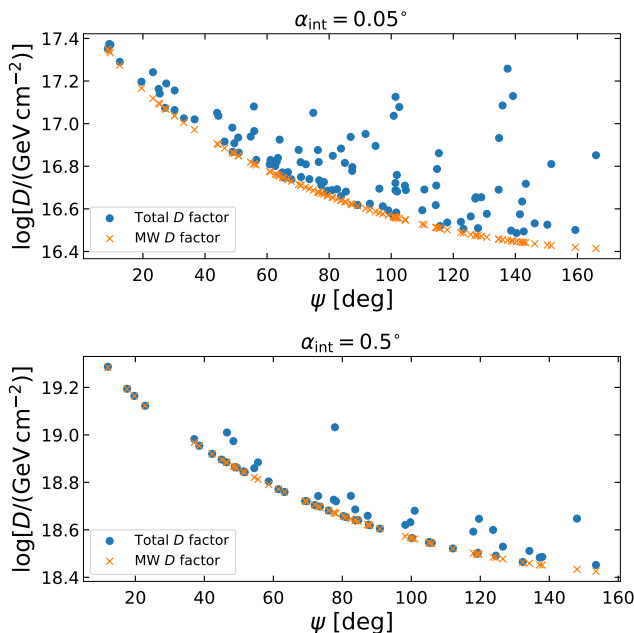


FIG. 5. D factors generated by Monte Carlo simulations for mock LSST dSphs and contribution of the Milky-Way halo component as a function of angle ψ from the Galactic center. Top and bottom panels show two cases of different integration angle: $\alpha_{\text{int}} = 0.05^\circ$ and 0.5° , respectively. Orange crosses show the contribution of the Milky-Way halo, whereas the blue dots show the total D factor, i.e. the sum of the dSph and Milky-Way components.

With this flux, we can calculate the event counts in an energy bin between E_1 and E_2 with

$$N = T \int_{E_1}^{E_2} dE A_{\text{eff}}(E) \int dE' P(E, E') \frac{dF}{dE'}, \quad (9)$$

where $P(E, E')$ takes the detector energy resolution into account as a probability of assigning an energy E to an event with true energy E' , $A_{\text{eff}}(E)$ is the effective area of the detector, and T is its exposure time. For the energy resolution, we adopt a normal distribution:

$$P(E, E') = \frac{1}{\sqrt{2\pi}\sigma_E} \exp\left[-\frac{(E - E')^2}{2\sigma_E^2}\right], \quad (10)$$

which is characterized by detector specific value of σ_E . For Athena, XRISM, and eROSITA, they have an energy resolution in terms of the full width at the half maximum (FWHM $\equiv 2\sqrt{2\ln 2}\sigma_E$) of 2.5 eV [27], 7 eV [26] and 138 eV [25], respectively. We summarize this and all the other relevant specifications for each of these detectors in Table I.

To the detector background in Table I (which are energy-independent in given units), we added a contribution coming from the cosmic X-ray background [49]. The contribution depends on X-ray photon energy, which becomes significant at lower energies compared with the detector background.

In order to assess sensitivity to sterile neutrino decays, for each detector, we generate mock data set (n_i ; the subscript i runs over different energy bins) through Monte Carlo simulations with Poisson distribution assuming null hypothesis, where there is no dark matter component (i.e., $\Gamma = 0$). The theoretically predicted signal and background counts in each bin i , as a function of decay width Γ is then marked as $\mu_i(\Gamma)$. The likelihood, i.e., the probability of obtaining the mock data n_i given the parameter Γ , is then calculated as a product of Poisson probability mass functions with the mean $\mu_i(\Gamma)$, $P[n_i|\mu_i(\Gamma)]$:

$$\mathcal{L}(\Gamma) = \prod_i P[n_i|\mu_i(\Gamma)] = \prod_i \frac{\mu_i(\Gamma)^{n_i} e^{-\mu_i(\Gamma)}}{n_i!}. \quad (11)$$

The test statistic (TS) used in the prediction of the decay rate is defined as:

$$\text{TS}(\Gamma) = -2 \ln \left[\frac{\mathcal{L}(\Gamma)}{\mathcal{L}_{\text{max}}} \right], \quad (12)$$

where \mathcal{L}_{max} refers to the maximum likelihood, and the corresponding decay width would be the best fit parameter Γ_0 . An acceptable hypothesis of decay width with 95% confidence level (CL) requires $\text{TS} \leq 2.71$, which determines that the upper limit of the decay rate appears when $\text{TS} = 2.71$.

A. Results for pointing instruments: XRISM and Athena

In Sec. III A, we discussed the distribution of D factors for each known dSph, based on which a Monte-Carlo sample is generated. Randomly choosing a value from the sample of D factors, we calculate a corresponding 95% CL upper limit on Γ_{ν_s} . We repeat this procedure and obtain distribution of the Γ_{ν_s} upper limit. With Eq. (7), the results are then converted to the limits on $\sin^2 2\theta$. Figure 6 shows the 95% CL upper limits on $\sin^2 2\theta$ as a function of sterile neutrino masses m_{ν_s} both for XRISM and Athena, which would be obtained by observing two dSphs, Draco (left) and Ursa Major II (right). The thick and thin bands show 68% and 95% containment regions, respectively, around the medians shown with curves in the middle. The uncertainties come from both those of D factor estimates and the Poisson fluctuation of the X-ray photon count. We also show the best-fit parameter region of claimed 3.5-keV X-ray line [8], and this study clearly shows that the claim can be definitely assessed with these future instruments by looking at promising dSphs.

In this work, following Ref. [38], in order to obtain the D -factor distribution of the ultrafaint dSphs, we modeled subhalos based on cold dark matter framework. Sterile neutrinos, however, are considered instead to behave as warm dark matter, where small-scale structures tend to

TABLE I. Summary of specifications for Athena [27], XRISM [26] and eROSITA [25].

	Athena	XRISM	eROSITA
Energy resolution (FWHM)	2.5 eV	7 eV	138 eV
Effective area at 3.5 keV	4367 cm ²	219 cm ²	554 cm ²
Detector background	5.8×10^3 keV ⁻¹ s ⁻¹ sr ⁻¹	2×10^3 keV ⁻¹ s ⁻¹ FOV ⁻¹	1151 keV ⁻¹ s ⁻¹ sr ⁻¹
Angular resolution	2.5 arcmin	1.7 arcmin (HPD)	< 15'' on axis (HEW @ 1.5 keV)
Field of view (FOV)	5 arcmin (diameter)	2.9×2.9 arcmin ²	0.833 deg ²

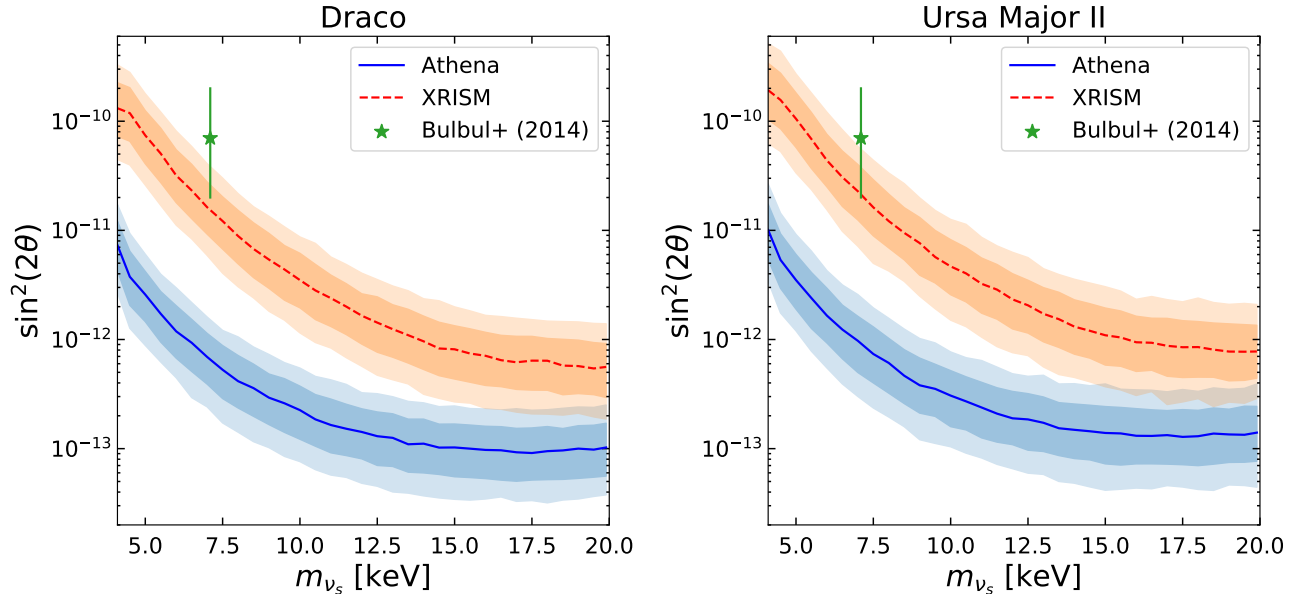


FIG. 6. Upper limits (95% CL) on mixing angle θ as a function of sterile neutrino mass m_{ν_s} for XRISM and Athena using D -factor distribution from Draco (left) and Ursa Major II (right). The thick and thin bands show 68% and 95% containment regions, respectively, accommodating uncertainty of D factor for each dSph as well as the Poisson fluctuation of the X-ray photon counts. In both panels, the half opening angle for Athena is 2.5 arcmin, while for XRISM, 1.64 arcmin. The best-fit parameter region for claimed possible 3.5 keV line [8] is also shown for comparison.

be erased. This will impact the constraints on the mixing angle through prior distribution of density profile and hence of D factors. However, satellite-formation condition, which we parameterized as V_{peak} thresholds is little known. As they both change the number of small and faint satellites, the effect of warm dark matter power spectrum is entirely degenerate with the V_{peak} threshold. To this end, we effectively test the impact of warm dark matter power spectrum by adopting larger values of V_{peak} threshold such as 18 and 22 km s⁻¹, shown in Fig. 7 for the ultrafaint dSph Ursa Major II. We find very little dependence on different satellite forming conditions through different values of V_{peak} threshold, well within the uncertainty bands shown in Fig. 6. This justifies that the model of cold dark matter subhalos combined with phenomenological treatment of satellite formation can be used to discuss sterile neutrino constraints with dSphs.

B. Results for all-sky instrument: eROSITA

For eROSITA that enables all-sky survey, we consider both known dSphs and potential LSST sources. We perform a joint-likelihood analysis of all available dSphs using an integration angle of $\alpha_{\text{int}} = 0.5^\circ$. The subscript i in Eq. (11) now runs over each dSph in the sample as well as energy bin. In Fig. 8, we show expected sensitivity to the mixing angle $\sin^2 2\theta$ for a given mass m_{ν_s} , expected with all the known and future LSST dSphs. These show that both the known and future LSST dSphs can be used to test the claim of 7 keV sterile neutrino [11], although the X-ray photon counts might fluctuate upward to prevent the solid conclusion. Since the angular resolution of eROSITA is much better than the aperture of 0.5° that we considered here, we also repeated the same analysis but by dividing the regions of interest around each dSph into ten equal-width annuli. We however find that this hardly changes the quantitative conclusion. This is because the characteristic of the signal and the background is very different already in their energy distributions, and hence, adding one more degree of discriminating them

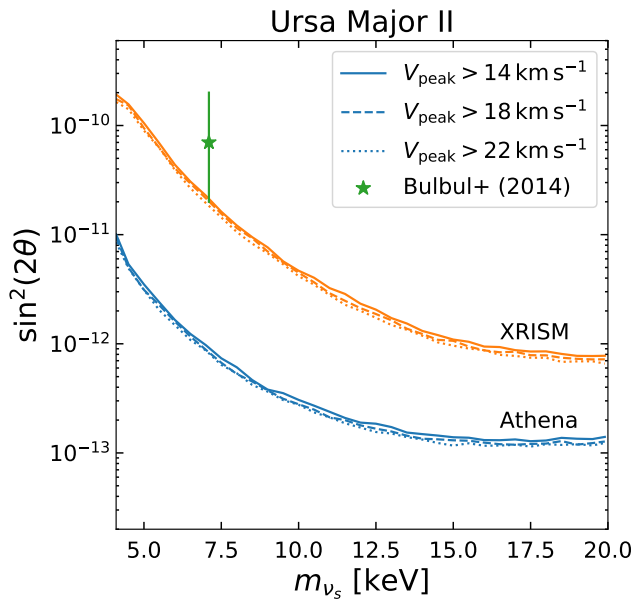


FIG. 7. Mixing angle constraints for Athena and XRISM with Ursa Major II ultrafaint dSph, where only medians are shown for different satellite formation conditions parameterized with V_{peak} .

does not help improve the eROSITA’s sensitivity any further.

V. HEAVY DARK MATTER

For heavy dark matter, we consider candidates χ decaying into $b\bar{b}$ or $\tau^+\tau^-$ channels. Once a heavy dark matter particle decays, the daughter particles hadronize and one of the byproducts is gamma rays that can be detected with the gamma-ray observatories such as HAWC and CTA. We here consider the masses of these dark matter candidates to be in the range of 200 TeV–20 PeV. To calculate the expected gamma-ray event spectrum for a given source, we use the PPPC4DMID numerical package [50] for calculating the particle spectrum of dark matter decay for aforementioned channels with a maximum possible dark matter mass of 200 TeV. For masses above 200 TeV, we use the energy scaling proposed in Ref. [51]:

$$\frac{dN}{dE} = \frac{m_A}{m_\chi} \frac{dN_A}{dE'} \quad (E' = E \frac{m_A}{m_\chi}), \quad (13)$$

where $m_A = 200$ TeV is the reference mass and dN_A/dE is the spectrum calculated at m_A . The obtained spectrum is used to calculate the gamma-ray flux from dark matter decay using Eq. (1). We then use the gamma-ray flux to calculate the expected amount of events for an energy bin of a detector using Eq. (9). This section targets the detection of gamma-ray flux for heavy dark matter searches within the gamma-ray energy range between 300 GeV and 100 TeV.

TABLE II. Summary of specifications considered for HAWC and CTA.

	HAWC	CTA
Flat energy resolution	100%	10%
Minimal angular resolution	0.5°	0.05°
Exposure time ^a	2 years	500 hours [55]
Field of view (FOV) ^b	2/3 of sky	4.5–10°

^a To each source.

^b CTA comprises multiple telescopes with different FOVs, and its overall FOV depends on the array layout. HAWC is an all-sky telescope.

A major background contribution to gamma-ray detection in current telescopes comes from cosmic rays, specifically from energetic electrons (e) and protons (p). These fluxes are given as [52]

$$\frac{d^2\phi_e}{dEd\Omega} = 1.17 \times 10^{-11} \left(\frac{E}{\text{TeV}} \right)^{-\Gamma} (\text{GeV cm}^2 \text{ s sr})^{-1}, \quad (14)$$

$$\frac{d^2\phi_p}{dEd\Omega} = 8.73 \times 10^{-9} \left(\frac{E}{\text{TeV}} \right)^{-2.71} (\text{GeV cm}^2 \text{ s sr})^{-1}, \quad (15)$$

with

$$\Gamma = \begin{cases} 3.0, & E < 1 \text{ TeV}, \\ 3.7, & E > 1 \text{ TeV}, \end{cases} \quad (16)$$

with which the aforementioned procedure for calculating the events per energy bin per given solid angle are performed to evaluate the background contributions. For different observatories, we consider the relevant hadron efficiencies which are then corrected against the hadron background flux during our analysis. The hadron rejection factor along with the effective area (with G/H cut) for HAWC has been extracted from Ref. [53]. For CTA, we have considered an overall cutoff factor of 10^{-2} while shifting the energies by a pre-factor of 3 in order to account for the reduced Cherenkov light emitted by hadronic showers [54]. The effective areas for CTA telescopes are similarly extracted from www.cta-observatory.org. The relevant specifications further considered for corresponding telescopes are given in Table II.

In Fig. 9, we have presented gamma-ray event spectrum along with background events expected for each detector for a mock dark matter source with the D factors of 10^{19} and 10^{17} GeV cm^{-2} for HAWC ($\alpha_{\text{int}} = 0.5^\circ$) and CTA ($\alpha_{\text{int}} = 0.05^\circ$), respectively, $m_\chi = 200$ TeV, and $\Gamma_\chi = 10^{-28} \text{ s}^{-1}$.

In order to project detector sensitivities on dark matter lifetime, we adopt a similar procedure as adopted in the previous section for identifying mixing angle limits for sterile neutrino dark matter, by evaluating the likelihood and TS. In this particular case, signal and background counts ($\mu_i(\Gamma)$) for a range of dark matter decay rates (Γ_χ) at given dark matter mass (m_χ) are calculated for each

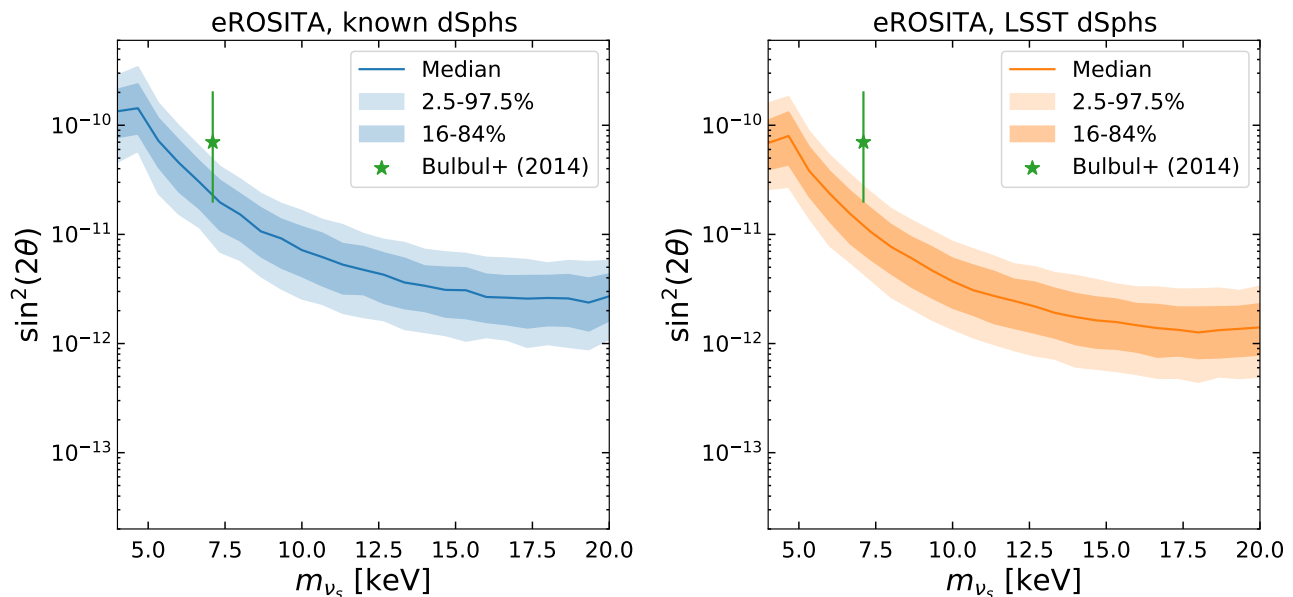


FIG. 8. Left: Mixing angle constraints for eROSITA using D -factor data from all known dwarfs. Right: Mixing angle constraints for eROSITA using prospective all-sky LSST sources. In both panels, the analysis is performed for a single annulus of 0.5° . For each mass, 500 Monte Carlo runs were performed.

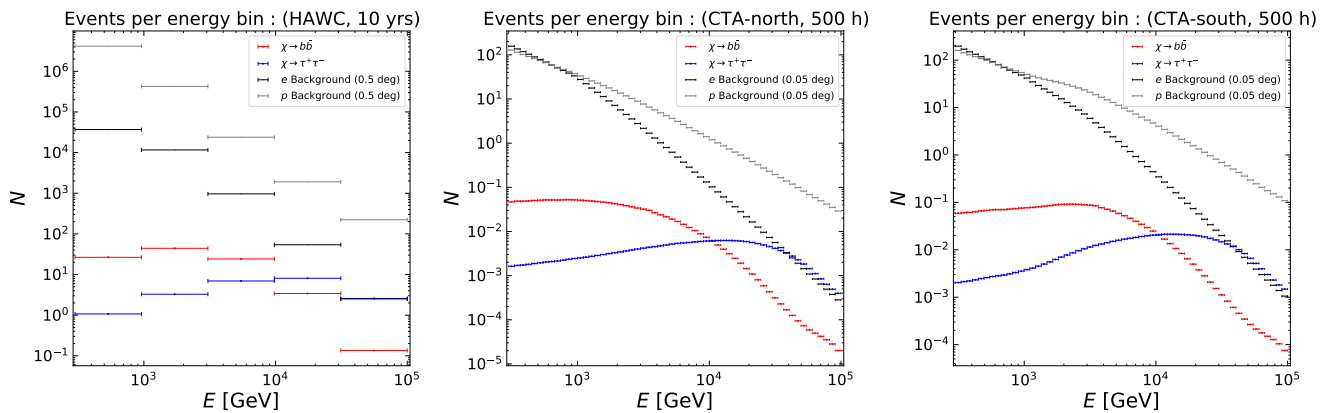


FIG. 9. Event counts per energy bin, proton and electron backgrounds for HAWC ($\alpha_{\text{int}} = 0.5^\circ$), CTA-north and CTA-south ($\alpha_{\text{int}} = 0.05^\circ$), while considering efficiency cutoffs for the hadron background contributions for each telescope. The dark matter parameters adopted are $m_\chi = 200$ TeV, $\Gamma_\chi = 10^{-28} \text{ s}^{-1}$, and $D = 10^{19} \text{ GeV cm}^{-2}$ (HAWC) and $D = 10^{17} \text{ GeV cm}^{-2}$ (CTA).

telescope as discussed above. We used the flat energy resolutions for these telescopes when calculating energy bins; i.e., the energy bin widths considered are constant in logarithm space. The next subsections present the obtained sensitivity limits of the considered heavy dark matter from both the HAWC and CTA.

A. Results for HAWC

In this subsection, we take 21 known dSphs, whose declination δ is within $\pm 45^\circ$ around the position of the HAWC, 19° [56] such that they are within HAWC's field of view. We correct for the exposure of the HAWC that

is the largest toward the zenith, by multiplying it by an extra factor of $\cos(\delta - 19^\circ)$. As it mainly surveys the northern sky, we do not discuss implications from the future LSST dSphs that will be mostly found in the southern sky. We consider a single detection annulus of 0.5° degree, corresponding to HAWC's minimal angular resolution. An extra step while finding the joint likelihood is to consider a sum of all log-likelihoods obtained from each candidates (dSphs) :

$$\ln \mathcal{L}(\Gamma) = \sum_{\text{dSph}} \ln \mathcal{L}_{\text{dSph}}(\Gamma), \quad (17)$$

from which the lower limits of decay lifetime with 95% CL, τ_{95} , are obtained similarly as in Sec. IV. For each

dark matter mass considered, we have obtained 1000 τ_{95} values to remedy any statistical anomalies in our computations.

In Fig. 10, we present the results for both $b\bar{b}$ and $\tau^+\tau^-$ decay channels for the considered known 21 dSphs. Individual likelihood analysis for each of the known dSphs is presented in Appendix (Fig. 15) presenting only the median values of the distribution of 1000 τ_{95} values obtained per dark matter mass. The HAWC's sensitivity is stronger than 10^{27} s nearly independent of mass for the $b\bar{b}$, while it gets reduced to 10^{26} s for the $\tau^+\tau^-$ if dark matter mass is heavier than ~ 10 PeV. This is because for dark matter in this mass range, most of the gamma-ray photons are emitted well above the energy range that we consider, as the spectrum for the $\tau^+\tau^-$ channel is much harder than the case of the $b\bar{b}$ channel.

B. Results for CTA

CTA will have much better angular resolution than HAWC. Taking advantage of this, within its field of view of $\sim 5\text{--}10^\circ$, one can have multiple annuli. Here we adopt 10 annuli, each of whose widths is 0.05° within the region with radius of 0.5° . However, since the field of view is limited to a narrow region of sky, we mainly focus on the few best target dSphs. Among the known dSphs, we discuss one classical dSph, Draco, and one ultrafaint dSph, Ursa Major II. Figure 11 shows the expected constraints on the dark matter lifetime with Draco and Ursa Major II, simulated for the CTA North for all both the $b\bar{b}$ and $\tau^+\tau^-$ decay channels. Here, we have again considered 1000 τ_{95} values per dark matter mass while computing the sensitivity bands. We find that the generic trend of these limits is the same as those obtained for HAWC, but the limits are overall slightly weaker. This is because of combined statistical power of all dSphs that can be seen with HAWC thanks to its large field of view, albeit its less good energy and angular resolution.

CTA South will survey the entire southern sky, which will allow us to observe dSphs detected with LSST. We consider through Monte Carlo simulations the best possible LSST dSph candidate that would possess the largest D factor from their host subhalo. The results are shown in Figure 12. The expected limits are stronger by a factor of a few than the case of Draco and Ursa Major II that can be observed with the CTA North.

VI. DISCUSSION AND CONCLUSIONS

In this paper, we made a comprehensive study of dark matter decays in the dwarf spheroidal galaxies. By revisiting their density profile estimates with the latest models of subhalo and satellite formation, we updated predictions of X-ray and gamma-ray fluxes from dwarf galaxies. We then discussed detectability of dark matter signals at X-ray telescopes (eROSITA, XRISM, and

Athena), if dark matter is made of sterile neutrinos with keV masses, and high-energy gamma-ray observatories (HAWC and CTA) if dark matter is made of metastable particles heavier than conventional WIMPs.

With physically motivated priors, we show that the posterior distributions of the astrophysical D -factors for dSphs are narrower, but are also typically lower compared to the case with uninformative prior. Such an effect was shown for the case of dark matter annihilation, but to a stronger degree [38]. With our revised estimates of the D -factors, our results are more robust, though also weaker than previously expected.

For pointing X-ray satellites, XRISM and Athena, we performed sensitivity estimates for two of the most promising dwarfs: Draco (classical) and Ursa Major II (ultrafaint). With both these instruments, we should be able to critically test much debated 3.5-keV X-ray lines, which suggested mixing angle of $\sin^2 2\theta = 7 \times 10^{-11}$ for 7.1 keV sterile neutrinos. The excellent energy resolution of these detectors will also allow the use of velocity spectroscopy as a detection diagnostic tool [57–59]. For the all-sky instrument, eROSITA, we are able to combine information of all the dwarfs. It is also sensitive to test the claimed 3.5-keV line for the current known dwarfs and also tens of ultrafaint dwarf galaxies that might be found with the LSST in the future.

The dwarf galaxies are among many other complementary target regions. Besides galaxies and clusters of galaxies that are already studied extensively [9, 11], the cosmic X-ray background [21, 24] and their anisotropies and cross correlations [60, 61] have also been proven to be efficient in constraining sterile neutrino dark matter. It would also be interesting to study the expected sensitivity of eROSITA with the Galactic halo analysis, by adopting, e.g., inner regions around the Galactic center (A. Dekker et al., in preparation).

For heavy dark matter, we explore the mass range between 200 TeV and 20 PeV that decays into $b\bar{b}$ or $\tau^+\tau^-$. We are able to probe the lifetime of the heavy dark matter in the range of $10^{27}\text{--}10^{28}$ s for the $b\bar{b}$ channel, whereas the limits are weaker for $\tau^+\tau^-$ channel for mass ranges greater than PeV. Both CTA and HAWC will yield similar sensitivity to the dark matter decay. Although HAWC has smaller effective area than CTA, it has a larger field of view that enables greater sky coverage. This enables joint likelihood analysis of all the dwarfs in its field of view, compensating its smaller effective area. In the future, once LHAASO is completed, it is expected to be more sensitive than HAWC due to its larger effective area and broader energy coverage.

If heavy dark matter decays to either $b\bar{b}$ or $\tau^+\tau^-$ as was investigated in this study, these final states create a number of lower energy photons through hadronic and electromagnetic cascades. This was studied in a broader multimessenger context in Refs. [6, 7, 62], which show comparable lower limits to the dark matter lifetime on the order of 10^{28} s or so. In addition, it is expected that future neutrino telescopes such as IceCube-Gen2

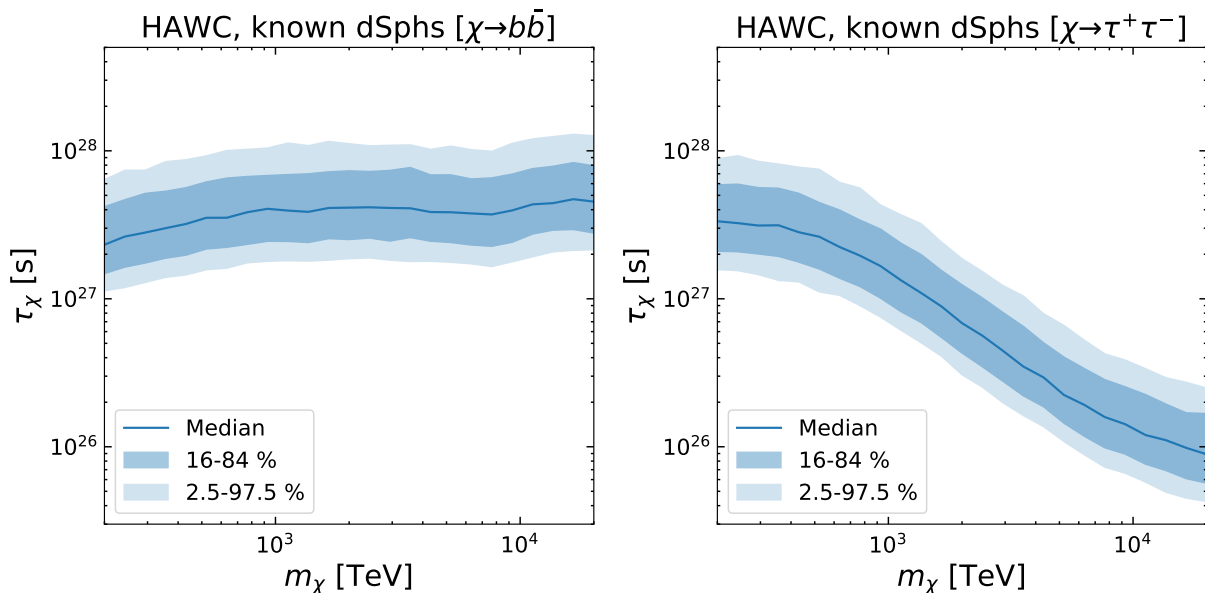


FIG. 10. Lower limits on dark matter decay lifetime from the joint likelihood analysis of 21 known dSphs that are within the field of view of HAWC. The constraints are given for both $\chi \rightarrow b\bar{b}$ channel (left) and $\chi \rightarrow \tau^+\tau^-$ channel (right). The median values are depicted as a solid line, and the 68% and 95% containment bands are shown in thick and thin relative shadings, respectively, as a result of the 1000 runs of obtaining mock data.

and KM3NeT are able to probe similar parameter regions [31, 32]. Therefore, both the HAWC and CTA will provide complementary constraints using other messengers.

ACKNOWLEDGMENTS

SA acknowledges the support by JSPS/MEXT KAKENHI Grant Numbers JP17H04836, JP18H04340, JP20H05850, and JP20H05861 (SA). KCYN was supported by the European Union’s Horizon 2020 research and innovation programme under the Marie Skłodowska-Curie grant agreement No 844664 (KCYN). This work was carried out over the two-month period in April and May 2020 in the MSc course, “Project Academic Skills for Research” at the University of Amsterdam. All the tasks were distributed to four sub-groups that worked on (a) D -factor estimates of known dwarfs (AGC, YM, INM); (b) D -factor estimates of LSST dwarfs (JK, MSPM, EP); (c) sterile neutrino constraints (ZF, SK, NMDS, FZ); and (d) heavy dark matter constraints (SKB, MF, CAvV), respectively, supervised by SA and KCYN.

Appendix A: Dark matter decay in known dwarf galaxies

In this section, we summarize the results of D factors for all the known dSphs that we studied. First, we provide the D -factor median and 68% confidence intervals in Tables III and IV for the classical dSphs and

TABLE III. D -factor medians and corresponding 68% credible intervals of the classical dSphs for $\alpha_{\text{int}} = 0.5^\circ$. The third column ($R_{D_{\text{MW}}}$) represents the relative contribution of the Milky Way to the total D -factor: $R_{D_{\text{MW}}} = D_{\text{MW}}/(D_{\text{MW}} + D_{\text{dSph}})$.

Name	Classical	$R_{D_{\text{MW}}}$
Sagittarius	$18.59^{+0.10}_{-0.09}$	0.81
Draco	$18.30^{+0.18}_{-0.21}$	0.68
Ursa Minor	$18.26^{+0.15}_{-0.18}$	0.67
Sculptor	$18.22^{+0.16}_{-0.20}$	0.71
Fornax	$18.06^{+0.09}_{-0.11}$	0.76
Sextans	$17.96^{+0.21}_{-0.23}$	0.79
Leo I	$17.76^{+0.23}_{-0.28}$	0.85
Carina	$17.69^{+0.29}_{-0.37}$	0.88
Leo II	$17.58^{+0.32}_{-0.38}$	0.90

Tables V and IV for all the ultrafaint dSphs, organized in descending order of D_{dSph} values. Tables III and V correspond to integration angles of $\alpha_{\text{int}} = 0.5^\circ$, while Tables IV and VI were obtained with $\alpha_{\text{int}} = 0.05^\circ$. Additionally, the relative contribution of the Milky-Way D factor is shown for all the dSphs as a fractional contribution $R_{D_{\text{MW}}} \equiv D_{\text{MW}}/(D_{\text{MW}} + D_{\text{dSph}})$. In the case of the classical dSphs, the posterior densities were only calculated by employing $V_{\text{peak}} > 25 \text{ km s}^{-1}$, while a few values of V_{peak} are explored for the ultrafaint dSphs.

Subsequently, in order to provide further visualization of the characteristics of the posterior distributions resulting from the parameter inference analysis, in Fig. 13 we present the D -factor posterior distributions as shown in

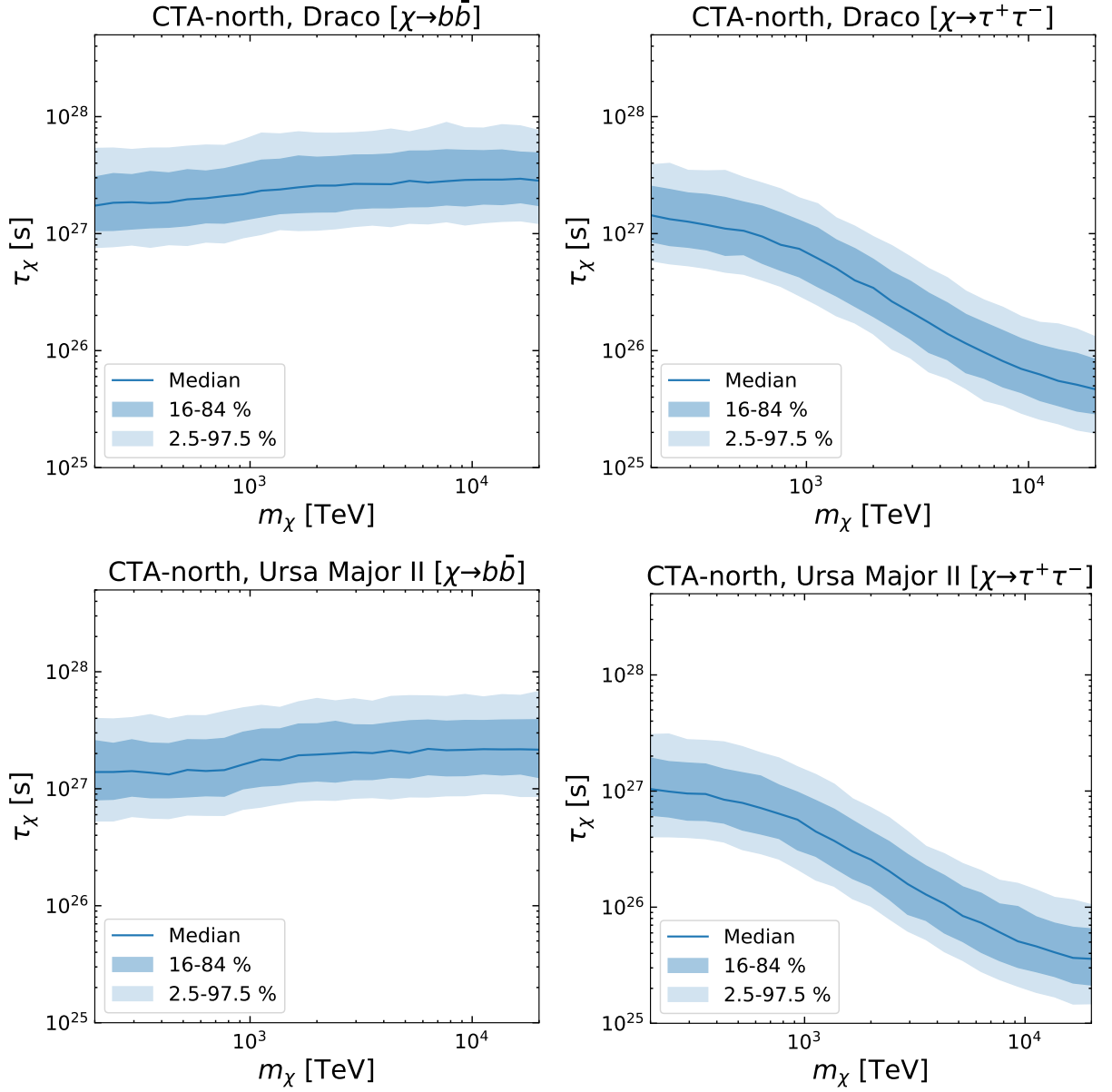


FIG. 11. Dark matter lifetime constraints for some the best known dSphs, Draco (top) and Ursa Major II (bottom), detectable with the CTA North telescopes, for the $b\bar{b}$ (left) and $\tau^+\tau^-$ (right) final states. The solid lines show the medians, while the light and dark bands show 68% and 95% containment intervals, respectively, as a result of the 1000 Monte Carlo simulations of mock data.

TABLE IV. The same as Table III, but for $\alpha_{\text{int}} = 0.05^\circ$.

Name	Classical	$R_{\mathcal{D}_{\text{MW}}}$
Sagittarius	$16.98^{+0.15}_{-0.15}$	0.64
Draco	$16.87^{+0.10}_{-0.11}$	0.36
Ursa Minor	$16.84^{+0.10}_{-0.10}$	0.35
Sculptor	$16.82^{+0.09}_{-0.10}$	0.39
Fornax	$16.74^{+0.10}_{-0.09}$	0.39
Sextans	$16.68^{+0.11}_{-0.12}$	0.41
Leo I	$16.62^{+0.04}_{-0.05}$	0.43
Carina	$16.56^{+0.12}_{-0.14}$	0.51
Leo II	$16.51^{+0.07}_{-0.07}$	0.52

Fig. 1 for some of the most promising dwarf galaxies for $\alpha_{\text{int}} = 0.5^\circ$.

Lastly, we provide the constraints on the sterile neutrino mixing angle $\sin^2 2\theta$ for the eROSITA, and dark matter lifetime for the HAWC, resulting from the individual likelihood analysis of the known dSphs in Figs. 14 and 15, respectively. In these figures, We show only the medians of the constraints. These figures demonstrates that the overall constraints are much improved by gathering the statistical power of each individual dSph analyses.

TABLE V. D -factor medians and 68% credible intervals of the ultrafaint dSphs for $\alpha_{\text{int}} = 0.5^\circ$ and the different values of V_{peak} . $R_{D_{\text{MW}}}$ represents the relative contribution of the Milky Way to the total D -factor: $R_{D_{\text{MW}}} = D_{\text{MW}}/(D_{\text{MW}} + D_{\text{dSph}})$.

Name	$V_{\text{peak}} > 14 \text{ km s}^{-1}$	$R_{D_{\text{MW}}}$	$V_{\text{peak}} > 18 \text{ km s}^{-1}$	$R_{D_{\text{MW}}}$	$V_{\text{peak}} > 22 \text{ km s}^{-1}$	$R_{D_{\text{MW}}}$
Segue 1	18.27 ^{+0.22} _{-0.34}	0.63	18.32 ^{+0.21} _{-0.33}	0.60	18.40 ^{+0.21} _{-0.35}	0.56
Ursa Major II	18.25 ^{+0.20} _{-0.26}	0.62	18.29 ^{+0.18} _{-0.25}	0.60	18.38 ^{+0.16} _{-0.26}	0.54
Draco II	18.08 ^{+0.32} _{-0.47}	0.76	18.16 ^{+0.29} _{-0.47}	0.73	18.29 ^{+0.28} _{-0.42}	0.66
Reticulum II	18.07 ^{+0.25} _{-0.39}	0.77	18.11 ^{+0.26} _{-0.39}	0.75	18.17 ^{+0.28} _{-0.41}	0.73
Coma Berenices	18.03 ^{+0.21} _{-0.30}	0.79	18.06 ^{+0.22} _{-0.31}	0.77	18.15 ^{+0.30} _{-0.52}	0.74
Ursa Major I	17.96 ^{+0.20} _{-0.21}	0.77	18.00 ^{+0.32} _{-0.54}	0.75	18.11 ^{+0.25} _{-0.33}	0.70
Tucana II	17.86 ^{+0.31} _{-0.54}	0.89	17.94 ^{+0.29} _{-0.52}	0.88	18.07 ^{+0.34} _{-0.55}	0.84
Triangulum II	17.84 ^{+0.40} _{-0.63}	0.81	17.91 ^{+0.39} _{-0.60}	0.78	18.07 ^{+0.28} _{-0.47}	0.71
Bootes II	17.82 ^{+0.38} _{-0.69}	0.89	17.90 ^{+0.36} _{-0.63}	0.87	18.06 ^{+0.16} _{-0.25}	0.82
Carina II	17.74 ^{+0.34} _{-0.43}	0.88	17.78 ^{+0.36} _{-0.57}	0.87	17.86 ^{+0.37} _{-0.69}	0.85
Hydrus 1	17.65 ^{+0.30} _{-0.32}	0.92	17.71 ^{+0.37} _{-0.73}	0.91	17.79 ^{+0.37} _{-0.46}	0.90
Horologium I	17.64 ^{+0.38} _{-0.74}	0.90	17.64 ^{+0.30} _{-0.34}	0.90	17.62 ^{+0.28} _{-0.39}	0.91
Bootes I	17.62 ^{+0.24} _{-0.24}	0.93	17.62 ^{+0.24} _{-0.25}	0.93	17.62 ^{+0.42} _{-0.77}	0.93
Canes Venatici I	17.51 ^{+0.15} _{-0.14}	0.93	17.52 ^{+0.15} _{-0.15}	0.93	17.59 ^{+0.23} _{-0.31}	0.92
Aquarius 2	17.44 ^{+0.40} _{-0.77}	0.95	17.50 ^{+0.40} _{-0.76}	0.94	17.54 ^{+0.51} _{-0.59}	0.94
Canes Venatici II	17.38 ^{+0.36} _{-0.66}	0.94	17.41 ^{+0.38} _{-0.67}	0.94	17.50 ^{+0.20} _{-0.16}	0.93
Segue 2	17.31 ^{+0.54} _{-0.72}	0.93	17.36 ^{+0.55} _{-0.67}	0.93	17.50 ^{+0.44} _{-0.75}	0.90
Grus I	17.12 ^{+0.62} _{-1.09}	0.98	17.25 ^{+0.59} _{-1.06}	0.97	17.48 ^{+0.54} _{-1.04}	0.95
Eridanus II	17.10 ^{+0.31} _{-0.42}	0.97	17.17 ^{+0.53} _{-1.05}	0.96	17.36 ^{+0.53} _{-1.05}	0.94
Pisces II	17.07 ^{+0.54} _{-1.06}	0.97	17.16 ^{+0.29} _{-0.48}	0.97	17.31 ^{+0.41} _{-0.27}	0.96
Leo T	17.02 ^{+0.37} _{-0.60}	0.97	17.09 ^{+0.34} _{-0.62}	0.96	17.28 ^{+0.53} _{-1.04}	0.94
Leo V	16.99 ^{+0.60} _{-1.05}	0.98	17.09 ^{+0.58} _{-1.03}	0.97	17.27 ^{+0.58} _{-1.04}	0.95
Tucana III	16.94 ^{+0.54} _{-0.39}	0.98	17.06 ^{+0.56} _{-1.08}	0.98	17.23 ^{+0.36} _{-0.56}	0.97
Hercules	16.93 ^{+0.54} _{-0.61}	0.99	17.05 ^{+0.49} _{-0.35}	0.99	17.20 ^{+0.36} _{-0.70}	0.98
Pegasus III	16.93 ^{+0.59} _{-1.05}	0.98	16.87 ^{+0.56} _{-0.59}	0.98	16.83 ^{+0.78} _{-0.79}	0.99
Leo IV	16.78 ^{+0.73} _{-0.87}	0.99	16.81 ^{+0.74} _{-0.86}	0.98	16.75 ^{+0.61} _{-0.53}	0.99

TABLE VI. The same as Table V but for $\alpha_{\text{int}} = 0.05^\circ$.

Name	$V_{\text{peak}} = 14 \text{ km s}^{-1}$	$R_{D_{\text{MW}}}$	$V_{\text{peak}} = 18 \text{ km s}^{-1}$	$R_{D_{\text{MW}}}$	$V_{\text{peak}} = 22 \text{ km s}^{-1}$	$R_{D_{\text{MW}}}$
Segue 1	16.77 ^{+0.16} _{-0.18}	0.35	16.79 ^{+0.15} _{-0.17}	0.34	16.85 ^{+0.14} _{-0.17}	0.31
Ursa Major II	16.75 ^{+0.15} _{-0.17}	0.34	16.77 ^{+0.14} _{-0.15}	0.33	16.83 ^{+0.13} _{-0.15}	0.30
Ursa Major I	16.65 ^{+0.11} _{-0.12}	0.41	16.66 ^{+0.21} _{-0.23}	0.40	16.77 ^{+0.18} _{-0.22}	0.34
Coma Berenices	16.63 ^{+0.13} _{-0.15}	0.48	16.66 ^{+0.10} _{-0.11}	0.46	16.72 ^{+0.15} _{-0.17}	0.43
Draco II	16.62 ^{+0.21} _{-0.25}	0.48	16.65 ^{+0.12} _{-0.14}	0.46	16.71 ^{+0.19} _{-0.23}	0.43
Reticulum II	16.62 ^{+0.16} _{-0.18}	0.49	16.65 ^{+0.15} _{-0.18}	0.47	16.70 ^{+0.09} _{-0.10}	0.44
Tucana II	16.54 ^{+0.20} _{-0.26}	0.64	16.58 ^{+0.19} _{-0.25}	0.62	16.68 ^{+0.18} _{-0.22}	0.56
Bootes II	16.51 ^{+0.23} _{-0.23}	0.62	16.56 ^{+0.22} _{-0.29}	0.59	16.67 ^{+0.20} _{-0.26}	0.53
Triangulum II	16.48 ^{+0.22} _{-0.27}	0.49	16.53 ^{+0.22} _{-0.26}	0.46	16.65 ^{+0.20} _{-0.22}	0.39
Carina II	16.46 ^{+0.16} _{-0.20}	0.59	16.49 ^{+0.22} _{-0.29}	0.57	16.60 ^{+0.19} _{-0.28}	0.51
Horologium I	16.44 ^{+0.22} _{-0.31}	0.60	16.48 ^{+0.16} _{-0.19}	0.58	16.53 ^{+0.15} _{-0.17}	0.55
Canes Venatici I	16.41 ^{+0.05} _{-0.05}	0.62	16.42 ^{+0.10} _{-0.11}	0.61	16.47 ^{+0.20} _{-0.28}	0.59
Bootes I	16.41 ^{+0.10} _{-0.12}	0.67	16.41 ^{+0.12} _{-0.12}	0.67	16.45 ^{+0.10} _{-0.11}	0.65
Hydrus 1	16.39 ^{+0.12} _{-0.12}	0.68	16.41 ^{+0.05} _{-0.05}	0.67	16.44 ^{+0.10} _{-0.10}	0.66
Aquarius 2	16.34 ^{+0.21} _{-0.30}	0.70	16.39 ^{+0.20} _{-0.30}	0.68	16.42 ^{+0.19} _{-0.27}	0.66
Canes Venatici II	16.33 ^{+0.19} _{-0.25}	0.65	16.36 ^{+0.18} _{-0.26}	0.63	16.42 ^{+0.04} _{-0.05}	0.60
Segue 2	16.23 ^{+0.24} _{-0.23}	0.63	16.29 ^{+0.22} _{-0.21}	0.60	16.40 ^{+0.19} _{-0.16}	0.54
Eridanus II	16.22 ^{+0.16} _{-0.17}	0.68	16.26 ^{+0.29} _{-0.41}	0.66	16.39 ^{+0.27} _{-0.36}	0.59
Grus I	16.19 ^{+0.29} _{-0.43}	0.79	16.25 ^{+0.26} _{-0.42}	0.77	16.36 ^{+0.25} _{-0.39}	0.72
Pisces II	16.17 ^{+0.28} _{-0.44}	0.75	16.24 ^{+0.14} _{-0.17}	0.72	16.35 ^{+0.11} _{-0.09}	0.66
Leo T	16.17 ^{+0.20} _{-0.25}	0.67	16.21 ^{+0.18} _{-0.26}	0.65	16.33 ^{+0.25} _{-0.41}	0.58
Leo V	16.14 ^{+0.29} _{-0.42}	0.74	16.20 ^{+0.27} _{-0.44}	0.71	16.32 ^{+0.27} _{-0.39}	0.65
Pegasus III	16.13 ^{+0.28} _{-0.46}	0.78	16.20 ^{+0.27} _{-0.42}	0.75	16.30 ^{+0.16} _{-0.27}	0.71
Tucana III	16.13 ^{+0.17} _{-0.14}	0.80	16.19 ^{+0.16} _{-0.12}	0.78	16.30 ^{+0.14} _{-0.20}	0.73
Hercules	16.11 ^{+0.19} _{-0.24}	0.86	16.12 ^{+0.20} _{-0.22}	0.86	16.18 ^{+0.27} _{-0.33}	0.84
Leo IV	16.06 ^{+0.28} _{-0.38}	0.78	16.10 ^{+0.29} _{-0.37}	0.76	16.14 ^{+0.19} _{-0.21}	0.74

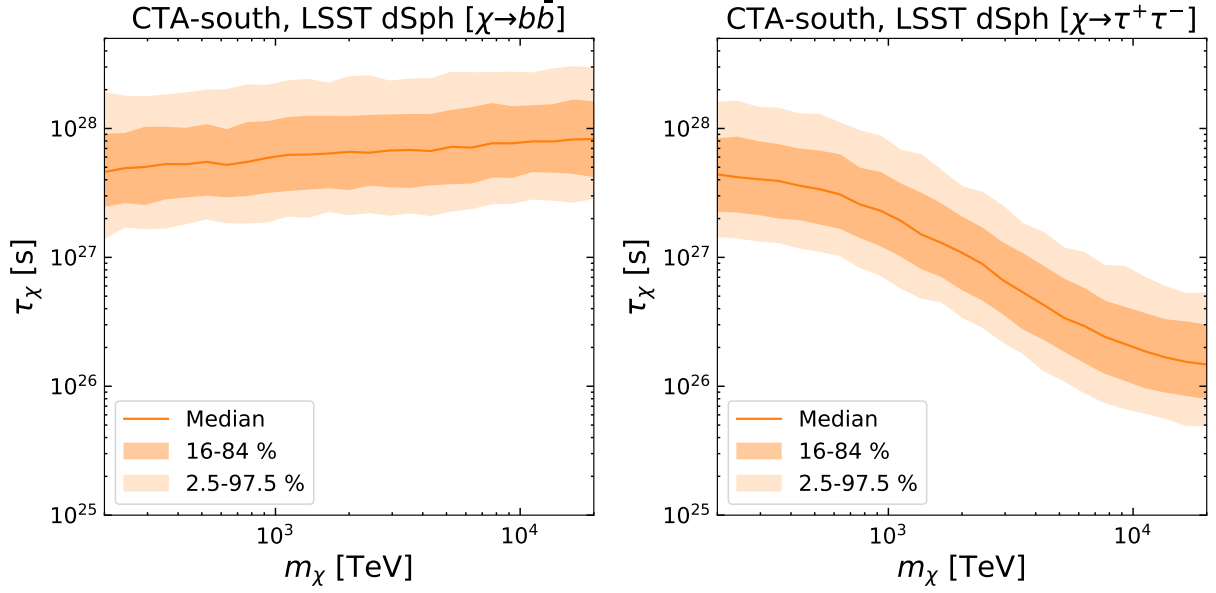


FIG. 12. The same as Fig. 11, but for a dSph with the largest D factor that would be detected with the LSST.

- [1] L. Roszkowski, E. M. Sessolo and S. Trojanowski, *WIMP dark matter candidates and searches—current status and future prospects*, *Rept. Prog. Phys.* **81** (2018) 066201, [[1707.06277](#)].
- [2] R. K. Leane, T. R. Slatyer, J. F. Beacom and K. C. Y. Ng, *GeV-scale thermal WIMPs: Not even slightly ruled out*, *Phys. Rev. D* **98** (2018) 023016, [[1805.10305](#)].
- [3] A. Boyarsky, M. Drewes, T. Lasserre, S. Mertens and O. Ruchayskiy, *Sterile Neutrino Dark Matter*, *Prog. Part. Nucl. Phys.* **104** (2019) 1–45, [[1807.07938](#)].
- [4] P. W. Graham, I. G. Irastorza, S. K. Lamoreaux, A. Lindner and K. A. van Bibber, *Experimental Searches for the Axion and Axion-Like Particles*, *Ann. Rev. Nucl. Part. Sci.* **65** (2015) 485–514, [[1602.00039](#)].
- [5] S. Tulin and H.-B. Yu, *Dark Matter Self-interactions and Small Scale Structure*, *Phys. Rept.* **730** (2018) 1–57, [[1705.02358](#)].
- [6] K. Ishiwata, O. Macias, S. Ando and M. Arimoto, *Probing heavy dark matter decays with multi-messenger astrophysical data*, *JCAP* **01** (2020) 003, [[1907.11671](#)].
- [7] K. Murase, R. Laha, S. Ando and M. Ahlers, *Testing the Dark Matter Scenario for PeV Neutrinos Observed in IceCube*, *Phys. Rev. Lett.* **115** (2015) 071301, [[1503.04663](#)].
- [8] E. Bulbul, M. Markevitch, A. Foster, R. K. Smith, M. Loewenstein and S. W. Randall, *Detection of An Unidentified Emission Line in the Stacked X-ray spectrum of Galaxy Clusters*, *Astrophys. J.* **789** (2014) 13, [[1402.2301](#)].
- [9] A. Boyarsky, O. Ruchayskiy, D. Iakubovskiy and J. Franse, *Unidentified Line in X-Ray Spectra of the Andromeda Galaxy and Perseus Galaxy Cluster*, *Phys. Rev. Lett.* **113** (2014) 251301, [[1402.4119](#)].
- [10] T. E. Jeltema and S. Profumo, *Discovery of a 3.5 keV line in the Galactic Centre and a critical look at the origin of the line across astronomical targets*, *Mon. Not. Roy. Astron. Soc.* **450** (2015) 2143–2152, [[1408.1699](#)].
- [11] E. Bulbul, M. Markevitch, A. R. Foster, R. K. Smith, M. Loewenstein and S. W. Randall, *Comment on “Dark matter searches going bananas: the contribution of Potassium (and Chlorine) to the 3.5 keV line”*, [[1409.4143](#)].
- [12] T. Jeltema and S. Profumo, *Reply to Two Comments on “Dark matter searches going bananas the contribution of Potassium (and Chlorine) to the 3.5 keV line”*, [[1411.1759](#)].
- [13] D. Malyshev, A. Neronov and D. Eckert, *Constraints on 3.55 keV line emission from stacked observations of dwarf spheroidal galaxies*, *Phys. Rev. D* **90** (2014) 103506, [[1408.3531](#)].
- [14] T. Tamura, R. Iizuka, Y. Maeda, K. Mitsuda and N. Y. Yamasaki, *An X-ray Spectroscopic Search for Dark Matter in the Perseus Cluster with Suzaku*, *Publ. Astron. Soc. Jap.* **67** (2015) 23, [[1412.1869](#)].
- [15] HITOMI collaboration, F. Aharonian et al., *Hitomi constraints on the 3.5 keV line in the Perseus galaxy cluster*, *Astrophys. J. Lett.* **837** (2017) L15, [[1607.07420](#)].
- [16] K. Perez, K. C. Y. Ng, J. F. Beacom, C. Hersh, S. Horiuchi and R. Krivonos, *Almost closing the ν MSM sterile neutrino dark matter window with NuSTAR*, *Phys. Rev. D* **95** (2017) 123002, [[1609.00667](#)].
- [17] N. Cappelluti, E. Bulbul, A. Foster, P. Natarajan, M. C. Urry, M. W. Bautz et al., *Searching for the 3.5 keV Line in the Deep Fields with Chandra: the 10 Ms observations*, *Astrophys. J.* **854** (2018) 179, [[1701.07932](#)].
- [18] K. C. Y. Ng, B. M. Roach, K. Perez, J. F. Beacom, S. Horiuchi, R. Krivonos et al., *New Constraints on Sterile Neutrino Dark Matter from NuSTAR M31*

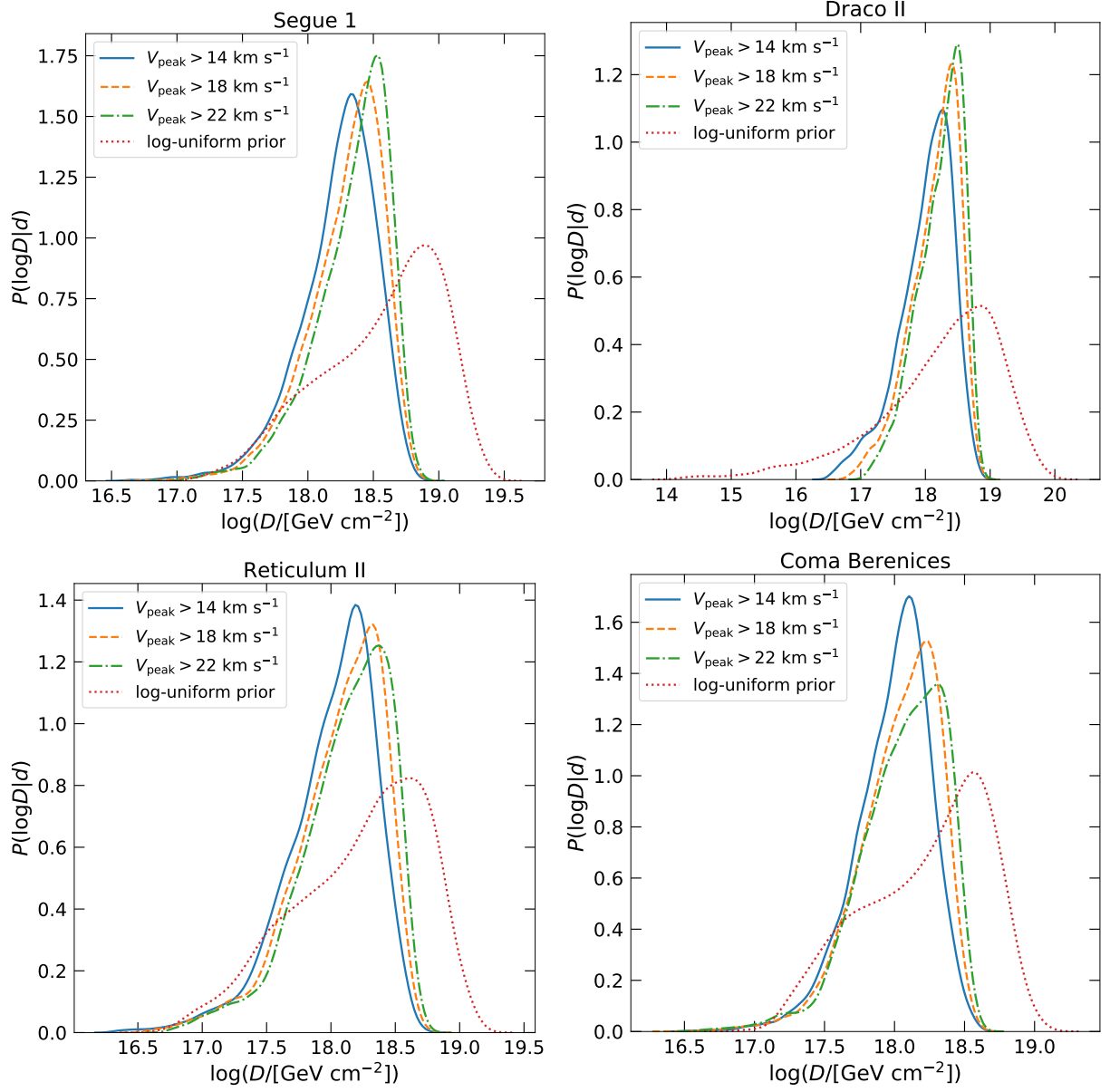


FIG. 13. Posterior distributions of $D_{\text{dSph}}(0.5^\circ)$ for Segue 1, Draco II, Reticulum II, Coma Berenices, and Ursa Major I, obtained with satellite priors with $V_{\text{peak}} > 14 \text{ km s}^{-1}$ (solid), $V_{\text{peak}} > 18 \text{ km s}^{-1}$ (dashed), $V_{\text{peak}} > 22 \text{ km s}^{-1}$ (dot-dashed), and log-uniform priors (dotted).

- Observations, *Phys. Rev. D* **99** (2019) 083005, [1901.01262].
- [19] B. M. Roach, K. C. Y. Ng, K. Perez, J. F. Beacom, S. Horiuchi, R. Krivonos et al., *NuSTAR Tests of Sterile-Neutrino Dark Matter: New Galactic Bulge Observations and Combined Impact*, *Phys. Rev. D* **101** (2020) 103011, [1908.09037].
- [20] A. C. Gall, A. R. Foster, R. Silwal, J. M. Dreiling, A. Borovik, E. Kilgore et al., *EBIT Observation of Ar Dielectronic Recombination Lines Near the Unknown Faint X-Ray Feature Found in the Stacked Spectrum of Galaxy Clusters*, *Astrophys. J.* **872** (2019) 194, [1902.01234].
- [21] C. Dessert, N. L. Rodd and B. R. Safdi, *The dark matter interpretation of the 3.5-keV line is inconsistent with blank-sky observations*, *Science* **367** (2020) 1465, [1812.06976].
- [22] K. N. Abazajian, *Technical Comment on "The dark matter interpretation of the 3.5-keV line is inconsistent with blank-sky observations"*, 2004.06170.
- [23] A. Boyarsky, D. Malyshev, O. Ruchayskiy and D. Savchenko, *Technical comment on the paper of Dessert et al. "The dark matter interpretation of the 3.5 keV line is inconsistent with blank-sky observations"*, 2004.06601.
- [24] J. W. Foster, M. Kongsore, C. Dessert, Y. Park, N. L. Rodd, K. Cranmer et al., *A deep search for decaying dark matter with XMM-Newton blank-sky observations*,

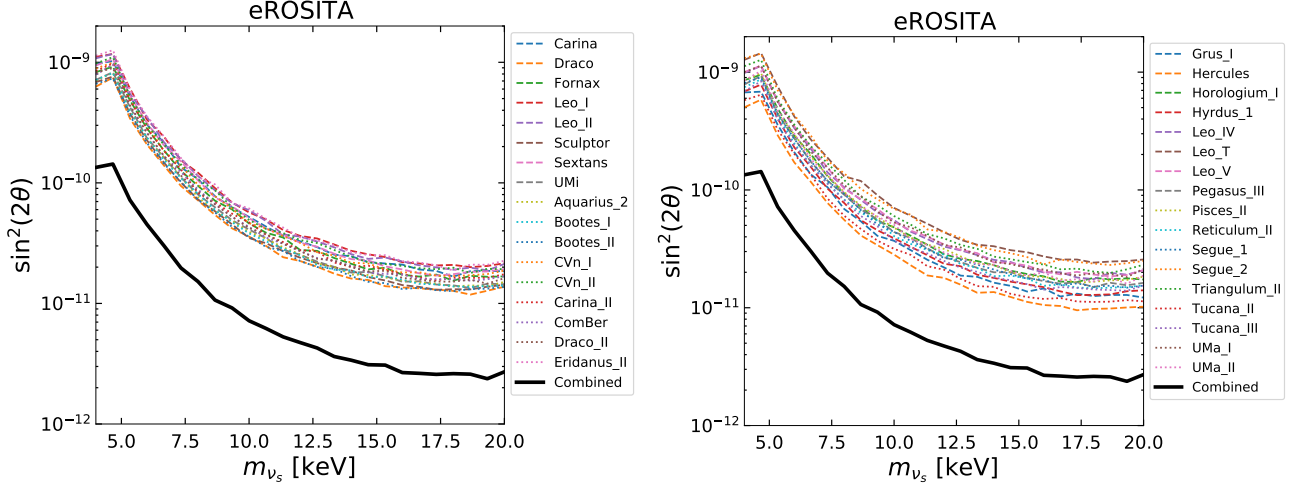


FIG. 14. Medians of the mixing angle constraints with $\alpha_{\text{int}} = 0.5^\circ$ for eROSITA computed for individual dSphs compared with the combined limits (thick solid).

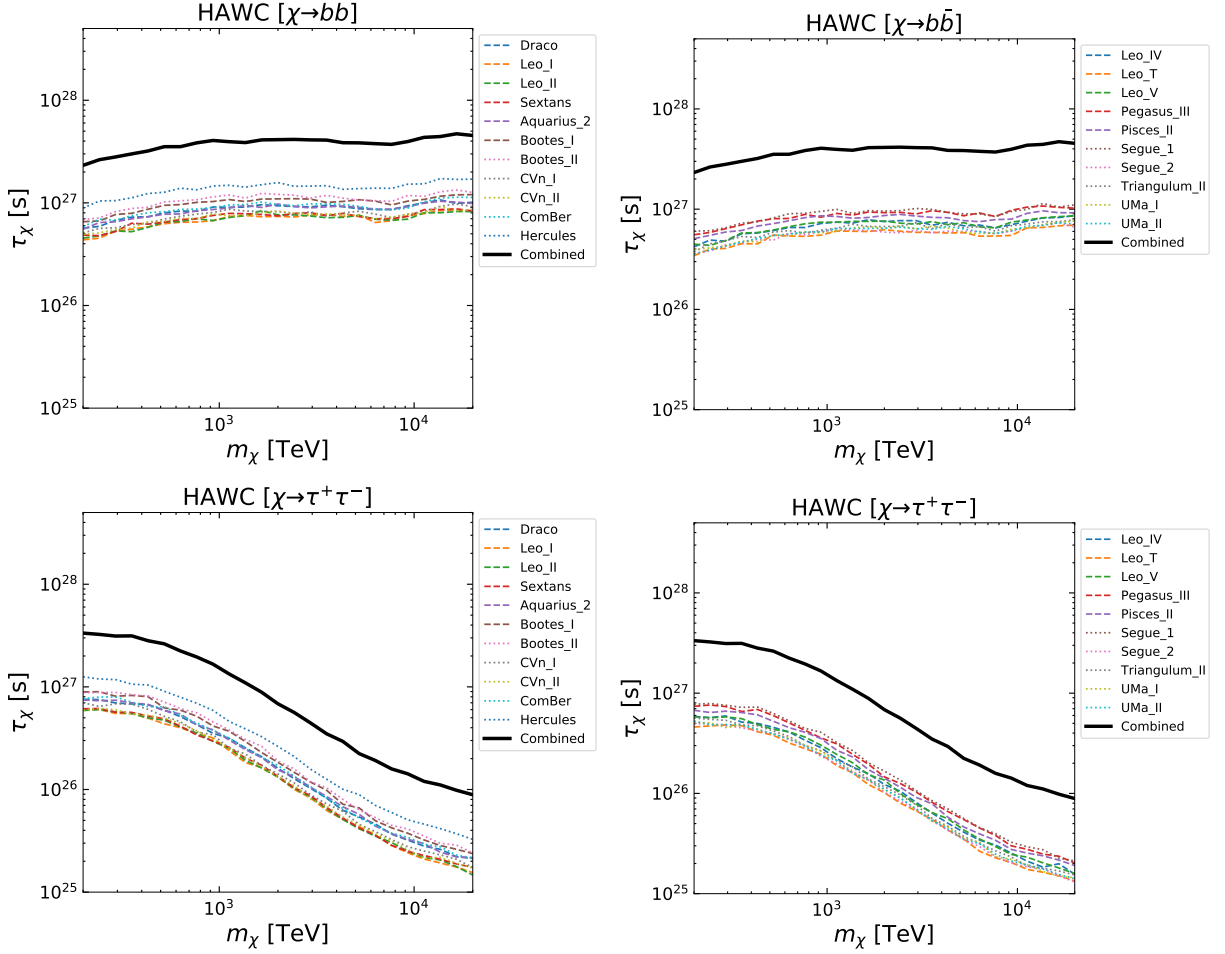


FIG. 15. Medians of the dark matter lifetime constraints with $\alpha_{\text{int}} = 0.5^\circ$ for HAWC computed for individual dSphs compared with the combined limits (thick solid). Top and bottom panels show the results of $b\bar{b}$ and $\tau^+\tau^-$ final states, respectively.

- 2102.02207.
- [25] EROSITA collaboration, A. Merloni et al., *eROSITA Science Book: Mapping the Structure of the Energetic Universe*, [1209.3114](#).
- [26] XRISM SCIENCE TEAM collaboration, *Science with the X-ray Imaging and Spectroscopy Mission (XRISM)*, [2003.04962](#).
- [27] D. Barret et al., *The Athena X-ray Integral Field Unit*, *Proc. SPIE Int. Soc. Opt. Eng.* **10699** (2018) 106991G, [[1807.06092](#)].
- [28] HAWC collaboration, A. Albert et al., *Dark Matter Limits From Dwarf Spheroidal Galaxies with The HAWC Gamma-Ray Observatory*, *Astrophys. J.* **853** (2018) 154, [[1706.01277](#)].
- [29] CTA CONSORTIUM collaboration, J. Knödlseeder, *The Cherenkov Telescope Array*, in *16th Rencontres du Vietnam: Theory meeting experiment: Particle Astrophysics and Cosmology*, 4, 2020. [2004.09213](#).
- [30] X. Bai et al., *The Large High Altitude Air Shower Observatory (LHAASO) Science White Paper*, [1905.02773](#).
- [31] A. Dekker, M. Chianese and S. Ando, *Probing dark matter signals in neutrino telescopes through angular power spectrum*, *JCAP* **09** (2020) 007, [[1910.12917](#)].
- [32] K. C. Ng et al., *Sensitivities of KM3NeT on decaying dark matter*, [2007.03692](#).
- [33] A. Abeysekara et al., *Observation of the Crab Nebula with the HAWC Gamma-Ray Observatory*, *Astrophys. J.* **843** (2017) 39, [[1701.01778](#)].
- [34] F. Aharonian et al., *The observation of the Crab Nebula with LHAASO-KM2A for the performance study*, *Chin. Phys. C* **45** (2021) 025002, [[2010.06205](#)].
- [35] LHAASO collaboration, *Performance of LHAASO-WCDA and Observation of Crab Nebula as a Standard Candle*, [2101.03508](#).
- [36] LSST DARK MATTER GROUP collaboration, A. Drlica-Wagner et al., *Probing the Fundamental Nature of Dark Matter with the Large Synoptic Survey Telescope*, [1902.01055](#).
- [37] S. Ando et al., *Discovery prospects of dwarf spheroidal galaxies for indirect dark matter searches*, *JCAP* **1910** (2019) 040, [[1905.07128](#)].
- [38] S. Ando, A. Geringer-Sameth, N. Hiroshima, S. Hoof, R. Trotta and M. G. Walker, *Structure Formation Models Weaken Limits on WIMP Dark Matter from Dwarf Spheroidal Galaxies*, [2002.11956](#).
- [39] J. F. Navarro, C. S. Frenk and S. D. M. White, *A Universal density profile from hierarchical clustering*, *Astrophys. J.* **490** (1997) 493–508, [[astro-ph/9611107](#)].
- [40] N. W. Evans, J. L. Sanders and A. Geringer-Sameth, *Simple J-Factors and D-Factors for Indirect Dark Matter Detection*, *Phys. Rev.* **D93** (2016) 103512, [[1604.05599](#)].
- [41] M. Pato, F. Iocco and G. Bertone, *Dynamical constraints on the dark matter distribution in the Milky Way*, *JCAP* **12** (2015) 001, [[1504.06324](#)].
- [42] J. D. Simon, *The Faintest Dwarf Galaxies*, *Ann. Rev. Astron. Astrophys.* **57** (Aug., 2019) 375–415, [[1901.05465](#)].
- [43] A. Geringer-Sameth, S. M. Koushiappas and M. Walker, *Dwarf galaxy annihilation and decay emission profiles for dark matter experiments*, *Astrophys. J.* **801** (2015) 74, [[1408.0002](#)].
- [44] N. Hiroshima, S. Ando and T. Ishiyama, *Modeling evolution of dark matter substructure and annihilation boost*, *Phys. Rev. D* **97** (2018) 123002, [[1803.07691](#)].
- [45] T. Ishiyama, M. Enoki, M. A. Kobayashi, R. Makiya, M. Nagashima and T. Oogi, *The ν^2GC simulations: Quantifying the dark side of the universe in the Planck cosmology*, *Publ. Astron. Soc. Jap.* **67** (2015) 61, [[1412.2860](#)].
- [46] R. Makiya, M. Enoki, T. Ishiyama, M. A. R. Kobayashi, M. Nagashima, T. Okamoto et al., *The New Numerical Galaxy Catalog (ν^2GC): An updated semi-analytic model of galaxy and active galactic nucleus formation with large cosmological N-body simulations*, *Publ. Astron. Soc. Jap.* **68** (2016) 25, [[1508.07215](#)].
- [47] F. Calore, V. De Romeri, M. Di Mauro, F. Donato and F. Marinacci, *Realistic estimation for the detectability of dark matter sub-halos with Fermi-LAT*, *Phys. Rev. D* **96** (2017) 063009, [[1611.03503](#)].
- [48] S. Y. Kim, A. H. G. Peter and J. R. Hargis, *Missing Satellites Problem: Completeness Corrections to the Number of Satellite Galaxies in the Milky Way are Consistent with Cold Dark Matter Predictions*, *Phys. Rev. Lett.* **121** (2018) 211302, [[1711.06267](#)].
- [49] D. Lumb, R. Warwick, M. Page and A. De Luca, *X-ray background measurements with xmm-newton epic*, *Astron. Astrophys.* **389** (2002) 93, [[astro-ph/0204147](#)].
- [50] P. Ciafaloni, D. Comelli, A. Riotta, F. Sala, A. Strumia and A. Urbano, *Weak Corrections are Relevant for Dark Matter Indirect Detection*, *JCAP* **03** (2011) 019, [[1009.0224](#)].
- [51] M. Chianese, D. F. Fiorillo, G. Miele, S. Morisi and O. Pisanti, *Decaying dark matter at IceCube and its signature on High Energy gamma experiments*, *JCAP* **11** (2019) 046, [[1907.11222](#)].
- [52] H. Silverwood, C. Weniger, P. Scott and G. Bertone, *A realistic assessment of the CTA sensitivity to dark matter annihilation*, *JCAP* **03** (2015) 055, [[1408.4131](#)].
- [53] J. Goodman, *Sensitivity and Status of the HAWC Observatory*, in *33rd International Cosmic Ray Conference*, p. 0702, 1, 2016.
- [54] D. Fegan, *gamma/hadron separation at TeV energies*, *J. Phys. G* **23** (1997) 1013–1060.
- [55] CTA CONSORTIUM collaboration, B. S. Acharya et al., *Science with the Cherenkov Telescope Array*. WSP, 11, 2018, [10.1142/10986](#).
- [56] HAWC collaboration, A. Abeysekara et al., *On the sensitivity of the HAWC observatory to gamma-ray bursts*, *Astropart. Phys.* **35** (2012) 641–650, [[1108.6034](#)].
- [57] E. G. Speckhard, K. C. Y. Ng, J. F. Beacom and R. Laha, *Dark Matter Velocity Spectroscopy*, *Phys. Rev. Lett.* **116** (2016) 031301, [[1507.04744](#)].
- [58] D. Powell, R. Laha, K. C. Y. Ng and T. Abel, *Doppler effect on indirect detection of dark matter using dark matter only simulations*, *Phys. Rev. D* **95** (2017) 063012, [[1611.02714](#)].
- [59] D. Zhong, M. Valli and K. N. Abazajian, *Near to long-term forecasts in x-ray and gamma-ray bands: Are we entering the era of dark matter astronomy?*, *Phys. Rev. D* **102** (2020) 083008, [[2003.00148](#)].
- [60] F. Zandanel, C. Weniger and S. Ando, *The role of the eROSITA all-sky survey in searches for sterile neutrino dark matter*, *JCAP* **09** (2015) 060, [[1505.07829](#)].
- [61] A. Caputo, M. Regis and M. Taoso, *Searching for Sterile Neutrino with X-ray Intensity Mapping*, *JCAP* **03** (2020) 001, [[1911.09120](#)].

[62] T. Cohen, K. Murase, N. L. Rodd, B. R. Safdi and Y. Soreq, *γ -ray Constraints on Decaying Dark Matter*

and Implications for IceCube, *Phys. Rev. Lett.* **119** (2017) 021102, [[1612.05638](#)].